

Extreme submillimetre starburst galaxies

Michael Rowan-Robinson¹ ^{*}, Lingyu Wang², Duncan Farrah³, Dimitra Rigopoulou⁴,
Carlotta Gruppioni⁵, Mattia Vaccari⁶, Lucia Marchetti⁷, David L. Clements¹

¹*Astrophysics Group, Imperial College London, Blackett Laboratory, Prince Consort Road, London SW7 2AZ, UK*

²*SRON, Groningen 9747 AD, Netherlands*

³*Department of Physics, Virginia Tech, Blacksburg, VA 24061, USA*

⁴*Department of Astrophysics, University of Oxford, Keble Rd, Oxford OX1 3RH*

⁵*INAF, - Osservatorio Astronomico di Bologna, via Ranzani 1, I-40127 Bologna, Italy*

⁶*Astrophysics Group, University of the Western Cape, Private Bag X17, 7535, Bellville, Cape Town, South Africa*

⁷*Department of Physical Science, The Open University, Milton Keynes MK7 6AA, UK*

26 April 2017

ABSTRACT

We use two catalogues, a *Herschel* catalogue selected at 500 μm (HerMES) and an *IRAS* catalogue selected at 60 μm (RIFSCz), to contrast the sky at these two wavelengths.

Both surveys demonstrate the existence of extreme starbursts, with star-formation rates (SFRs) $> 5000 M_{\odot} \text{yr}^{-1}$. There appears to be a maximum (un-lensed) star-formation rate of 30,000 $M_{\odot} \text{yr}^{-1}$. *IRAS* sources with estimates higher than this are either lensed systems, blazars, or erroneous photometric redshifts.

At redshifts 3 to 5, the time-scale for the *Herschel* galaxies to make their current mass of stars at their present rate of formation $\sim 10^8 \text{ yrs}$, so these galaxies are making a significant fraction of their stars in the current star-formation episode. Using dust mass as a proxy for gas mass, the *Herschel* galaxies at redshift 3 to 5 have gas masses comparable to their mass in stars.

We have plotted here the individual spectral energy distributions (SEDs) for the 58 extreme starbursts in our *Herschel* survey, for which we have more complete SED information. Over 50% are QSOs or have an AGN dust torus, i.e. are Type 2 AGN, but in all cases the infrared luminosity is dominated by a starburst component. We derive a mean covering factor for AGN dust as a function of redshift and derive black hole masses and black hole accretion rates. There is a universal ratio of black-hole mass to stellar mass, $\sim 10^{-3}$, driven by the strong period of star-formation and black-hole growth at $z = 1-5$.

Key words: infrared: galaxies - galaxies: evolution - stars:formation - galaxies: starburst - quasars: supermassive black holes - cosmology: observations

1 INTRODUCTION

A key discovery of *IRAS* was the prevalence of very luminous starburst galaxies. Galaxies with infrared luminosities $> 10^{12} L_{\odot}$ were defined to be ultraluminous (Soifer et al 1984, Houck et al 1985), and those with luminosities $> 10^{13} L_{\odot}$ were defined to be hyperluminous (Rowan-Robinson et al 2000, Rowan-Robinson and Wang 2010). Submillimetre selected samples from *Herschel* show the existence of even more extreme objects (Rowan-Robinson et al 2016). Here we use infrared template modelling to select sources on the basis of their star-formation rate rather than

their infrared luminosity. Extreme starburst pose a problem for semi-analytic models of galaxy formation because the observed number-density of galaxies with star-formation rates $> 1000 M_{\odot} / \text{yr}$ substantially exceed the model predictions (Dowell et al 2014, Gruppioni et al 2015, Henriques et al 2015, Asboth et al 2016, Lacey et al 2016).

Two very different infrared surveys have highlighted the existence of extreme starbursts, with star-formation rates extending up to 30,000 M_{\odot} / yr . The Revised IRAS Faint Source Survey Redshift (RIFSCz) Catalogue (Wang et al 2014a) is a 60 μm survey for galaxies over the whole sky at $|b| > 20^{\circ}$, which incorporates data from SDSS, 2MASS, WISE, and *Planck* all-sky surveys to give wavelength coverage from 0.36–1380 μm . Since publication of Wang et al

^{*} E-mail: mrr@imperial.ac.uk

Table 1. RIFSCz catalogue by band

$\lambda(\mu\text{m})$	survey	no. of sources
3.4	WISE	48603
4.6	WISE	48603
12	WISE	48591
12	IRAS	4476
22	WISE	48588
25	IRAS	9608
60	IRAS	60303
65	AKARI	857
90	AKARI	18153
100	IRAS	30942
140	AKARI	3601
160	AKARI	739
350	PLANCK	2275
550	PLANCK	1152
850	PLANCK	616
1380	PLANCK	150

(2014a) *Akari* fluxes have been added to the catalogue, using a search radius of 1 arc min. An aperture correction needs to be applied to *Akari* 65 and 90 μm fluxes to give consistency with *IRAS* photometry (Rowan-Robinson and Wang 2015). The optical and near-infrared photometry of 1271 catalogued nearby galaxies has been improved, following a systematic trawl through the NASA/IPAC Extragalactic Database. Wang et al (2014) found that 93% of RIFSCz sources had optical or near infrared counterparts with spectroscopic or photometric redshifts. Table 1 summarises the number of RIFSCz galaxies by waveband.

The *HerMES* survey (Oliver et al 2012) allows us to construct a 500 μm sample of galaxies in areas in which we have optical and infrared data from the Spitzer-SWIRE survey (Rowan-Robinson et al 2014, 2016). Selection at 500 μm , rather than say 250 μm , gives us greater visibility of the high redshift universe and has the benefit of ensuring detection also at 350, and in most cases 250, μm , to give valuable SED information. The complete HerMES-SWIRE (Lockman+XMM+ES1+EN1+CDFS) 500 μm catalogue consists of 2181 galaxies, of which 275 are lensing candidates. In the Lockman+XMM+ES1 areas there are a further 833 good quality 500+350 μm sources which are not associated with Spitzer-SWIRE galaxies, for which Rowan-Robinson et al (2016) have estimated redshifts from their submillimetre colours. Table 2 contrasts the extragalactic sky as seen at 60 and 500 μm .

The COSMOS survey (Scoville et al 2007) area was also part of the HerMES SPIRE survey and the full COSMOS photometric survey has been published by Laigle et al (2016). Photometric redshifts have been discussed by Ilbert et al (2013) and Laigle et al (2016). Scoville et al (2016) have used these data to analyse gas masses and star formation rates from $z = 1-6$. The approach, based on monochromatic luminosities at 850 μm and CO (1-0) luminosities, glosses over the subtleties of variations of optical depth between sources which we try to capture through radiative transfer modelling of multi-wavelength SEDs (see also the discussion by Berta et al 2016). Pearson et al (2017) have used COSMOS data to discuss deblending and cross-identification issues for *Herschel* SPIRE data and, like Rowan-Robinson et

al (2014, 2016), use the optical to mid-infrared SED data to inform the association process. There are 181 500 μm sources with flux greater than 25 mJy, the flux limit we used in Rowan-Robinson et al (2016), and which also have 350 μm detections, in the 2.0 sq deg of the COSMOS survey. All have 24 μm associations. This yields a 500 μm source-density of 90 per sq deg, similar to that found in the 26.3 sq deg of our sample.

Schulz et al (2017) have published a new IPAC SPIRE catalogue (HPSC) which analyses data taken in all *Herschel* SPIRE programmes in a homogeneous way. This would appear to offer the opportunity of a much larger sample of SPIRE galaxies. We used the HPSC catalogue to create a 250-350-500 μm list as in Rowan-Robinson et al (2014). When we associated this list with the SWIRE photometric redshift catalogue (Rowan-Robinson et al 2013), we found only about half of the 2181 sources. This is an issue acknowledged in the HPSC explanatory supplement, which they attribute to blending of SPIRE sources in their detection procedure.

We also associated this HPSC 500 μm catalogue with RIFSCz, finding 1640 associations. Many of these were also detected by *Planck* and so we can make a direct comparison of 350 and 500 μm fluxes in the two surveys. We find that we need an aperture correction of $k \cdot \text{delmag}$, where $\text{delmag} = J_{\text{ext}} - J_{\text{ps}}$ is the J-band aperture correction and $k=0.15$ at 350, and 0.10 at 500 μm , to get agreement of SPIRE and *Planck* fluxes. Previously Wang et al (2014) reported the need for aperture corrections to be applied to WISE fluxes at 12 and 22 μm . The latest version of RIFSCz (<http://astro.ic.ac.uk/public/mrr/fss/readme>) thus provides a comprehensive collection of fluxes, with aperture corrections where necessary, from optical (SDSS), near infrared (2MASS), mid and far infrared (WISE, *IRAS*, *Akari*), through to submillimetre and millimetre (*Herschel* and *Planck*).

Section 2 of this paper discusses lensed galaxy diagnostics, section 3 discusses stellar mass, dust (and gas) masses and star formation rates, section 4 discusses extreme starbursts and section 5 discusses the role of AGN.

A cosmological model with $\Lambda=0.7$, $h_0=0.72$ has been used throughout. If we were to use $H_0 = 67 \text{ km/s/Mpc}$ (Planck 2015) luminosities and star-formation rates would be increased by 15.5%.

2 LENSED GALAXY DIAGNOSTICS

Table 2 shows a comparison of the sky seen at 60 and at 500 μm . The most striking aspects of 500 μm selection are (i) a much higher fraction of high redshift galaxies (Franceschini et al 1991), (ii) a much higher fraction of lensed objects (Blain et al 2002), (iii) a much higher fraction of galaxies with cool or cold dust (RR et al 2010, 2016, Rowan-Robinson and Clements 2015).

Figure 1 illustrates the 3.6-24-500 μm diagnostic ratios used by Rowan-Robinson et al (2014) to select lensed objects. It is a plot of S_{500}/S_{24} versus $S_{3.6}/S_{500}$, with candidate lensed objects shown in red, normal cirrus galaxies shown in black, galaxies with cool dust shown in blue and galaxies with cold dust shown in magenta. The colour selection shown, with

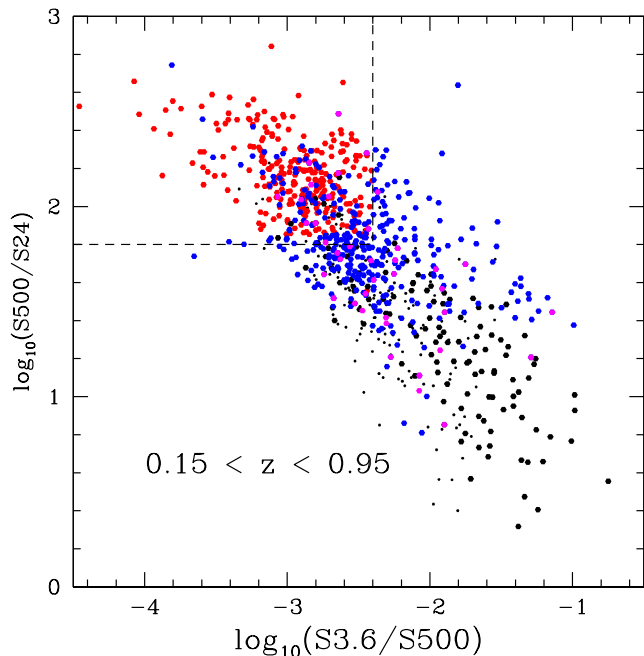


Figure 1. S24/S500 versus S3.6/S500 for Hermes-SWIRE galaxies (Lock+XMM+ES1+CDFS+EN1) with $0.15 < z < 0.95$. Red filled circles: lensing candidates, large black filled circles: galaxies with standard cirrus components, blue filled circles: galaxies with cool cirrus components, magenta filled circles: galaxies in Lockman (Rowan-Robinson et al 2014) with cold cirrus components, small black dots: non-cirrus galaxies.

Table 2. Contrast between 60 and 500 μm

	IRAS-FSS 60 μm	HerMES-SWIRE 500 μm
no. of sources	60303	2181
area (sq deg)	27143	26.3
Lensing surface-density	0.001 per sq deg	10 per sq deg
Ultraluminous	8 %	70%
Hyperluminous	0.7%	25%
Cirrus galaxies	42%	34%
of which, cooler dust	6%	85%
$z > 3$	4%	88%

others, is remarkably effective at identifying lensing candidates. Details of the table of the 275 HerMES-SWIRE (Lock+XMM+ES1+CDFS+EN1) lens candidates are given at <http://astro.ic.ac.uk/public/mrr/spiresfr/readmespirerev>

For IRAS FSS (RIFSCz) sources we can not use this colour-colour diagnostic. Instead the infrared luminosity, or inferred star-formation rate, is a good indicator of lensing. There do not seem to be any cases where the true, unlensed star-formation rate is $> 10^{4.5} M_{\odot}/\text{yr}$ (see section 3 and Fig 2R below). Table 3 lists 22 RIFSCz objects with the star-formation rate, calculated by the automated template-fitting code, $> 10^{4.5} M_{\odot}/\text{yr}^{-1}$. 4 are known lenses. One (F14218+3845) has been imaged with HST and shows no evidence of lensing (Farrah et al 2002): Rowan-Robinson and Wang (2010) point out that there is a discrepancy between the ISO 90 μm flux and the IRAS 60 and 100 μm

fluxes and if the former is adopted a much lower SFR ($4,400 M_{\odot}/\text{yr}$) is obtained. 3 are blazars, for which the submillimetre emission is non-thermal, one object is more probably associated with a $z=0.032$ Zwicky galaxy, and three have photometric redshifts > 4 which their SEDs show are implausible: these 7 have been removed from Fig 2R). We are left with 10 new candidate lenses, of which 5 have spectroscopic redshifts.

3 STELLAR MASS, DUST (AND GAS) MASS, STAR FORMATION RATE

Our approach of fitting optical and near infrared SEDs with templates based on stellar synthesis codes (Rowan-Robinson et al 2010, Babbedge et al 2010) allows us to estimate stellar masses, and fitting mid infrared, far infrared and submillimetre data with templates based on radiative transfer models (Rowan-Robinson et al 2010, 2013, 2016), allows us to estimate star formation rates and dust masses. In this paper we particularly focus on the very highest rates of star-formation found.

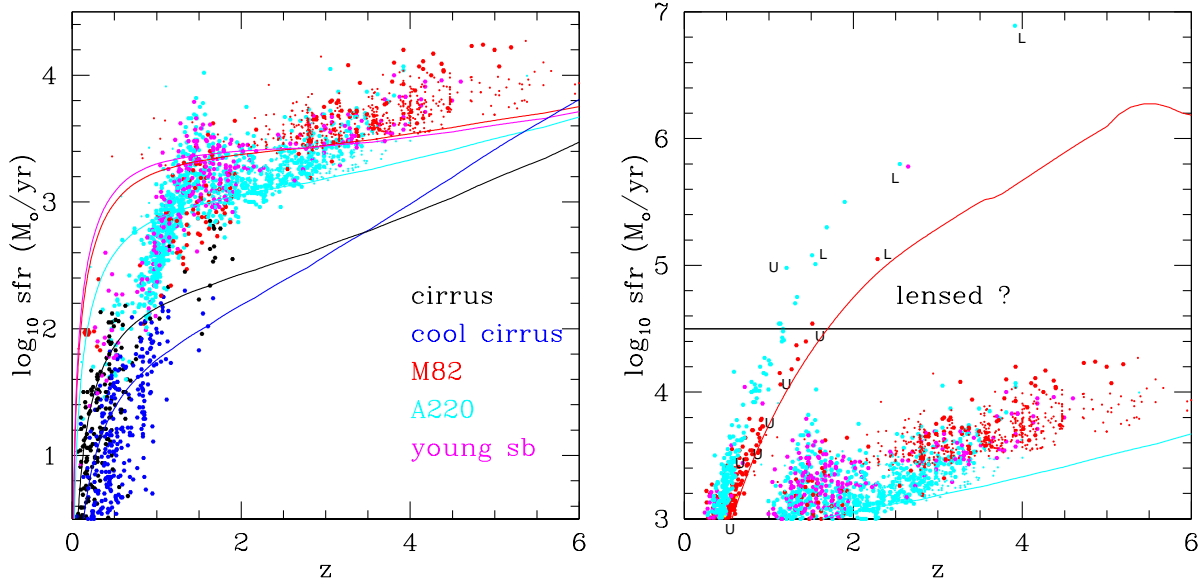
In the automated fitting of infrared SED templates and calculation of infrared luminosities and other derived quantities, we previously normalised the SEDs at 8 μm , if the source was detected there, or at 24 μm otherwise. In studying the SEDs of galaxies with very high star-formation rates, we have found that normalisation at 8 μm for sources at $z = 1.5-3.5$ can result in poor estimates of the infrared luminosity, because for many sources with $z > 1.5$ the 8 μm emission is dominated by starlight. For $z > 3.5$ we already required normalisation to be at 24 μm . We have therefore switched to normalisation at 24 μm for all sources. We can do this for this sample because we require a 24 μm detection in order to associate a *Herschel* source with a SWIRE photometric redshift catalogue source. This change significantly reduces the number of very high luminosity (and high star-formation rate) galaxies.

Figure 2L shows our revised plot of star-formation rate (SFR) against redshift for HerMES-SWIRE galaxies, which can be compared with Fig 2L of Rowan-Robinson et al (2016). Details of the revised HerMES-SWIRE catalogue are given at <http://astro.ic.ac.uk/public/mrr/spiresfr/readmespirerev>. These changes have some effect on the bright end of the star-formation rate functions (see appendix), but a negligible effect on the derived star-formation-rate density from $z = 0-6$.

Figure 2R shows the SFR against redshift for HerMES-SWIRE and RIFSCz galaxies with $\text{SFR} > 1000 M_{\odot}/\text{yr}$. Typical IRAS 60 μm and *Herschel* 500 μm detection limits are indicated. The highest star-formation rates significantly exceed the highest rates found by Weedman and Houck (2008) at $0 < z < 2.5$. There appears to be a natural upper limit to the SFR of $30,000 M_{\odot}/\text{yr}$. No HerMES-SWIRE galaxies are found above this value and the IRAS-FSS galaxies above this limit are probably gravitational lenses (see previous section and Table 3). This limit could represent an Eddington-type radiation pressure limit on the star-formation rate of the kind postulated by Elmegreen (1983), Scoville et al (2001), and Murray et al (2005). Scoville et al (2001) give a limit for L/M_{*} of 500 L_{\odot}/M_{\odot} , which would translate to $\text{SFR} < 10^{4.5} M_{\odot}/\text{yr}$ for $M_{*} < 10^{11.5} M_{\odot}$.

Table 3. Candidate lenses in Revised IRAS FSC Redshift Catalogue

name	RA	dec	z	nirtem	\log_{10} SFR	note
F02416-2833	40.953415	-28.343891	1.514000	2	4.54	
F03445-1359	56.718334	-13.844521	(1.14)	3	4.54	
F08105+2554	123.380363	25.750853	1.512380	3	5.08	L
F08177+4429	125.316353	44.333546	(2.65)	5	5.78	
F08279+5255	127.923744	52.754921	3.912200	3	6.89	L
F10018+3736	151.207672	37.362133	1.684160	3	5.30	
F10026+4949	151.469330	49.579998	1.120000	3	4.54	
F10119+1429	153.657822	14.251303	1.550000	3	5.01	
F10214+4724	156.144012	47.152695	2.285600	2	5.05	L
F10534+3355	164.055649	33.661686	(1.17)	3	4.50	
F13445+4128	206.656906	41.225357	(1.33)	3	4.75	
F13510+3712	208.286133	36.964321	1.311000	3	4.70	
F14132+1144	213.942673	11.495399	2.550000	3	5.80	L
F14218+3845	215.981201	38.530708	1.209510	3	4.98	U
F23265+2802	352.262146	28.312298	(1.90)	3	5.50	
F02263-0351	37.221718	-3.626988	2.055000	3	5.51	blazar
F00392+0853	10.453402	9.173513	(4.62?)	3	7.19?	alias at z=1.4
F06389+8355	102.896248	83.865295	(4.50?)	3	6.83?	alias at z=1.2
F13080+3237	197.619431	32.345490	0.998010	3	4.52	blazar
F15419+2751	236.008347	27.697693	(2.02)	3	5.55	Zwicky gal z=0.032
F16360+2647	249.522308	26.694941	(4.55?)	3	7.23?	z=0.066 2MASS gal at 0.27
F22231-0512	336.446899	-4.950383	1.404000	3	5.25	blazar 3C446

**Figure 2.** L: Star formation rate versus redshift for HerMES Lockman+XMM+ES1 galaxies, with 500 μm selection limits for each template type. R: Star-formation rate versus redshift for extreme starbursts. Data from HerMES Lockman+XMM+ES1 (Rowan-Robinson et al 2016) and from the IRAS RIFSCz catalogue (Wang et al 2014). Known lenses are indicated by L and cases known to be unlensed indicated by U (Farrah et al 2002). Typical 60 and 500 μm selection limits are indicated by the red and cyan loci.

We can use the dust mass as a proxy for gas mass, assuming a representative value for $M_{\text{gas}}/M_{\text{dust}}$. Magdis et al (2011) have summarised values of $M_{\text{gas}}/M_{\text{dust}}$ as a function of metallicity for local galaxies, and shown that a redshift 4 galaxy lies on the same relation, with $M_{\text{gas}} \sim 100M_{\text{dust}}$ (cf also Chen et al 2013). We use this ratio to estimate M_{gas} and then compare this with our stellar mass estimates. Figure 3L shows a plot of $(100 M_{\text{dust}})/M_*$ versus redshift for HerMES galaxies. For HerMES galaxies with $z > 1$, M_{gas} is

comparable with M_{stars} , so these are very gas-rich galaxies (as noted by Rowan-Robinson et al 2010). Very high gas fractions have been found in galaxies with $z > 1$ by Daddi et al (2010), Tacconi et al (2010, 2013), and Carrilli and Walter (2013). At low z , $100M_{\text{dust}} \sim 0.01 - 0.1M_*$ so these galaxies have consumed most of their gas in star-formation.

If we look at M_*/SFR as a function of z (Fig 3R), we see that the time to double the stellar mass at $z = 3-5$ is $\sim 10^8$ yrs. In some objects the gas-depletion time is as low

as $1\text{--}3 \times 10^7$ yrs (cf Rowan-Robinson 2000, Carilli and Walter 2013). The Scoville et al (2001) Eddington limit quoted above translates to $M_*/SFR \sim 10^7$ yrs.

The picture that emerges is that the *Herschel* galaxies at $z > 3$ are in the process of making most of the stars in the galaxy. Essentially these are metal factories. However we are not seeing monolithic galaxy formation of the kind postulated by Partridge and Peebles (1967), even though the star-formation rates and time-scales are similar to those they suggested, because we can see from the optical and near infrared SEDs that there has been an earlier generation of star-formation at least 1 Gyr prior to the star-formation we are witnessing. Between $z = 1$ and the present epoch we see a dramatic decline in the gas content and star-formation rate. For $z < 0.5$ the gas depletion time-scale is longer than the age of the universe so these are galaxies that must have had a much higher rate of star-formation in the past.

4 EXTREME STARBURSTS

Here we focus on galaxies with implied star-formation rates greater than $5000 M_\odot/\text{yr}$. Previously, detailed studies have been presented of just two objects in this class: Rowan-Robinson and Wang (2010) show the SED of one unlensed RIFSCz galaxy in this class (IRAS F15307+3252, $z = 0.926$) with $SFR = 5100 M_\odot/\text{yr}^{-1}$, and Dowell et al report an object (FLS1, $z = 4.29$) with $SFR = 9700 M_\odot/\text{yr}^{-1}$.

We show modelling of individual SEDs for all HerMES-SWIRE (Lock+XMM+ES1) galaxies with $SFR > 5000 M_\odot/\text{yr}^{-1}$. There are 66 in all (details given in Tables 3 and 4), but SED modelling shows that 8 of these have low-redshift aliases which are more likely. Rowan-Robinson et al (2016) showed that fitting our starburst templates to the 250–350–500 μm data gives an effective estimate of submillimetre redshift, z_{subm} . Combining the χ^2 distributions for the photometric and submillimetre redshifts gives a best fit combined redshift z_{comb} . Values of z_{subm} and z_{comb} are given in Tables 3 and 4. For a further 7 sources, z_{comb} is significantly less than z_{phot} and we have shown the SED with z_{comb} above the corresponding SED for z_{phot} . For these 7 the alternative SED did not seem a better fit than that for z_{phot} . Generally the SED fits for the 58 sources are plausible. Only 3 are based on spectroscopic redshifts and it would be desirable to obtain further spectroscopy.

Fig 4L shows SEDs of objects whose optical and near infrared data is fitted with a QSO template. Pitchford et al (2016) have studied 513 Type 1 QSOs detected by *Herschel* at 250 μm , some in the HerMES-SWIRE areas, and found star-formation rates ranging up to $5000 M_\odot/\text{yr}$, so there is almost no overlap with our sample. Fig 5 shows SEDs of objects whose optical-nir data is fitted with a galaxy template, but whose mid ir data show the presence of an AGN dust torus, i.e. these are Type 2 AGN. Altogether 30/58 objects are QSOs or Type 2 AGN. All of these have starburst components too and in no case does the luminosity in the AGN dust torus exceed that of the starburst.

Fig 6 shows SEDs of objects whose optical and near infrared data are fitted with galaxy templates and whose mid ir, far ir and submillimetre data are fitted with M82 or Arp220 starburst templates. Fig 4R shows galaxies whose mid and far infrared, and submillimetre, data are fitted

with young starburst templates. Altogether 28/58 objects are pure starbursts.

Star-formation rates in the range 5000–30,000 M_\odot/yr are not predicted by semi-analytic models of galaxy formation (Gruppioni et al 2015, Henriques et al 2015, Lacey et al 2016) and so these objects pose a serious challenge to theoretical models. Our 58 *Herschel*-SWIRE objects correspond to a surface density of 2.8 extreme starbursts per sq deg. 500 μm sources which are not associated with SWIRE galaxies could add a further ~ 9 extreme starbursts per sq deg.

5 ROLE OF AGN

A surprisingly high proportion of *Herschel* extreme starbursts have an AGN dust torus component (52%), though the dust tori are quite weak and in no case does L_{tor} exceed L_{sb} . Figure 7 shows the covering factor, $L_{\text{tor}}/L_{\text{opt}}$ versus redshift for SWIRE QSOs. Assuming the bolometric output of the black hole, $L_{\text{bh}} = 2.0 L_{\text{opt}}$ (RR et al 2009), the average covering factor, f , is ~ 0.4 for $z > 2$, declining to ~ 0.16 at $z = 0$. This trend can also be interpreted as a decline in dust torus covering factor with declining optical (and bolometric) luminosity (see Rowan-Robinson et al 2009 and references quoted therein). Using this relation, Fig 8L shows black-hole mass, $M_{\text{bh}}\beta^{-1}$, versus total stellar mass, M_* , for *Herschel* galaxies and for IRAS-FSS galaxies with $z < 0.3$, where M_{bh} is estimated from L_{bh} assuming that the AGN is radiating at a fraction β of the Eddington luminosity:

$$L_{\text{bh}} = \beta L_{\text{Edd}} = 4\pi\beta G M_{\text{bh}} m_p c / \sigma_T = 3.2 \times 10^4 \beta (M_{\text{bh}}/M_\odot) (L_\odot) \quad (1)$$

L_{bh} is estimated as $2.0 L_{\text{opt}}$ for QSOs, and from L_{tor}/f for galaxies with AGN dust tori. A wide range of values of the Eddington ratio β is found in the literature (Babic et al 2007, Fabian et al 2008, Steinhardt and Elvis 2009, Schutze and Wistotzki 2010, Suh et al 2015, Pitchford et al 2016), with a typical range of 0.01–1 for $z > 1$ (Kelly et al 2010, Lusso et al 2012).

Since QSOs are excluded from fig 8L by the requirement for a measurement of stellar mass, these are all Type 2 AGN. The mean value of $\lg_{10} L_{\text{bh}}/(\beta M_*)$ for 500 HerMES-SWIRE AGN is -4.11 , with an rms dispersion of 0.56.

Figure 8R shows $M_{\text{bh}}\beta^{-1}/M_*$ versus redshift for the same galaxies. If we take $\beta \sim 0.1$ as a characteristic value, then $M_{\text{bh}}/M_* \sim 0.001$ at all redshifts, with a range of ± 1 dex. This is reminiscent of the Magorrian et al (1998) relation between black-hole mass and bulge mass (see also review by Kormendy and Ho (2013)). This ratio is set by the very high star-formation (and black-hole build-up) at redshift 2–5. The Milky Way, with $M_* = 6.10^{10} M_\odot$ and $M_{\text{bh}} = 4.10^6 M_\odot$ lies in the lower end of this range.

Figure 9 shows M_{acc}/SFR versus redshift for *Herschel* galaxies and for (non-*Herschel*) SWIRE galaxies (smaller symbols), where the black-hole accretion rate M_{acc} is calculated assuming conversion efficiency of accreting mass to radiation is $\epsilon = 0.1$:

$$L_{\text{bh}} = \epsilon \dot{M}_{\text{acc}} c^2. \quad (2)$$

Note that the combination of equations (1) and (2) gives the Salpeter time-scale for black hole growth $t_S = 4.10^8 \epsilon \beta^{-1}$ yrs (Salpeter 1964). QSOs have been indicated in Fig 9 by open blue triangles.

While M_{acc}/SFR is $\sim 10^{-4}$ at $z = 2\text{--}5$, it is 30 times

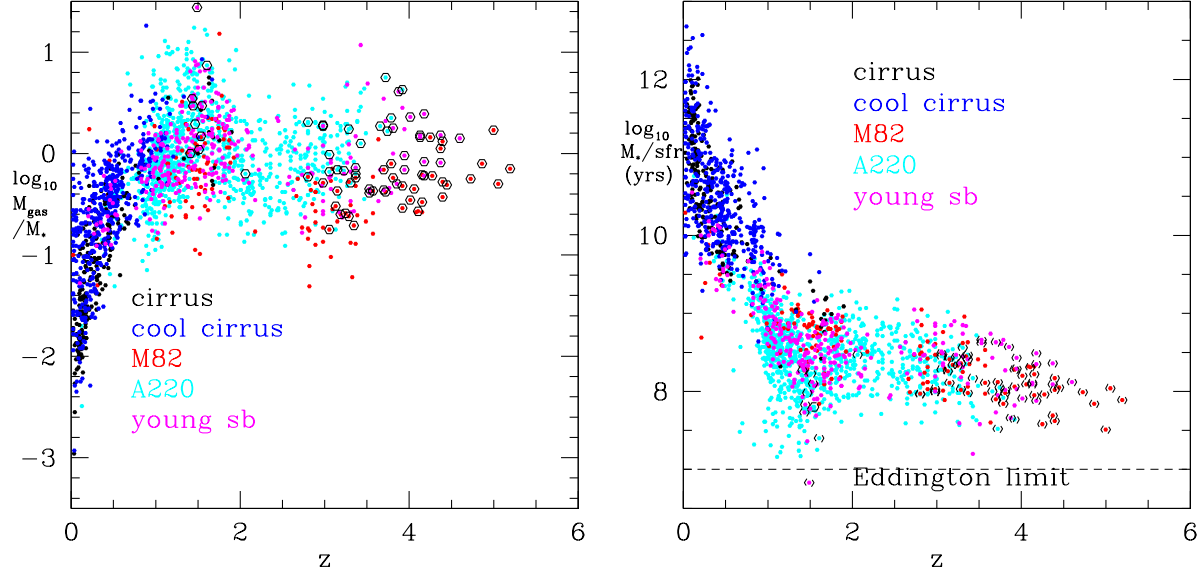


Figure 3. L: $M_{gas}(=100M_{dust})/M_*$ versus z . Circled points are extreme starbursts ($SFR > 5000 M_{\odot}/yr$). R: M_*/SFR (time-scale to make stars at present star-formation rate) versus z for HerMES galaxies, labelled with dominant infrared template type. Extreme starbursts ($SFR > 5000 M_{\odot} yr^{-1}$) are shown circled.

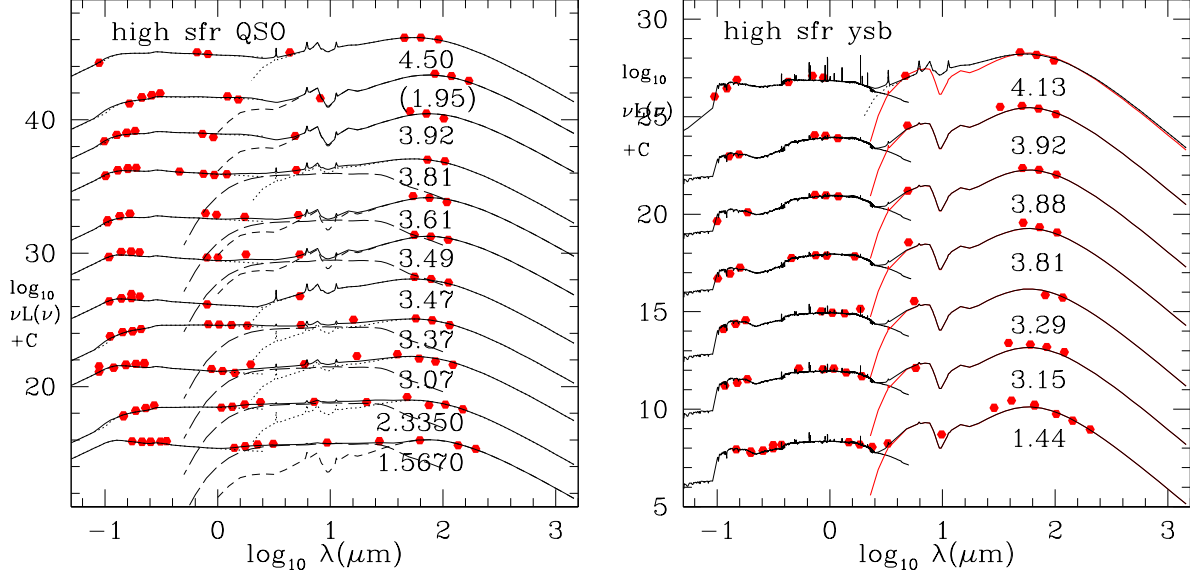


Figure 4. SEDs of Lockman-SPIRE 500 μm sources with extremes starburst luminosities labelled with the redshift, L: Optical-nearir fitted with QSO template. R: Farir-submm fitted with young starburst template. Lower redshift aliases (z_{comb}) are shown with redshift bracketed, above SED for the higher redshift alias. Dotted loci: M82 starburst, dashed loci: Arp 220 starburst, long-dashed loci: AGN dust torus, red loci: young starburst template.

higher at $z < 0.5$. The *IRAS* AGN (not shown) are consistent with low- z SWIRE galaxies. Barnett et al (2015) quote a much higher value of $M_{acc}/SFR \sim 0.2$ for a redshift 7.1 QSO, based on a SFR derived from the CII 158 μm line. However they also quote a bolometric luminosity of $6.7 \times 10^{13} L_{\odot}$, which could yield a SFR of $\sim 13,000 M_{\odot}/yr$, about 100 times their estimate from CII, and this would move M_{acc}/SFR into the range seen in Fig 9.

The star-formation rates in $z < 0.5$ galaxies are 1000

times lower than those seen in the extreme starbursts, but the black hole accretion rates are only 30 times lower. in these high redshift, high luminosity submillimetre galaxies we are presumably seeing major mergers (Chakrabarti et al 2008, Hopkins et al 2010, Haywards et al 2011, Ivison et al 2012, Aguirre et al 2013, Wiklind et al 2014, Chen et al 2015), in which the star formation is taking place close to the galactic nucleus, so it is not surprising that there is a strong connection between star-formation and black-hole

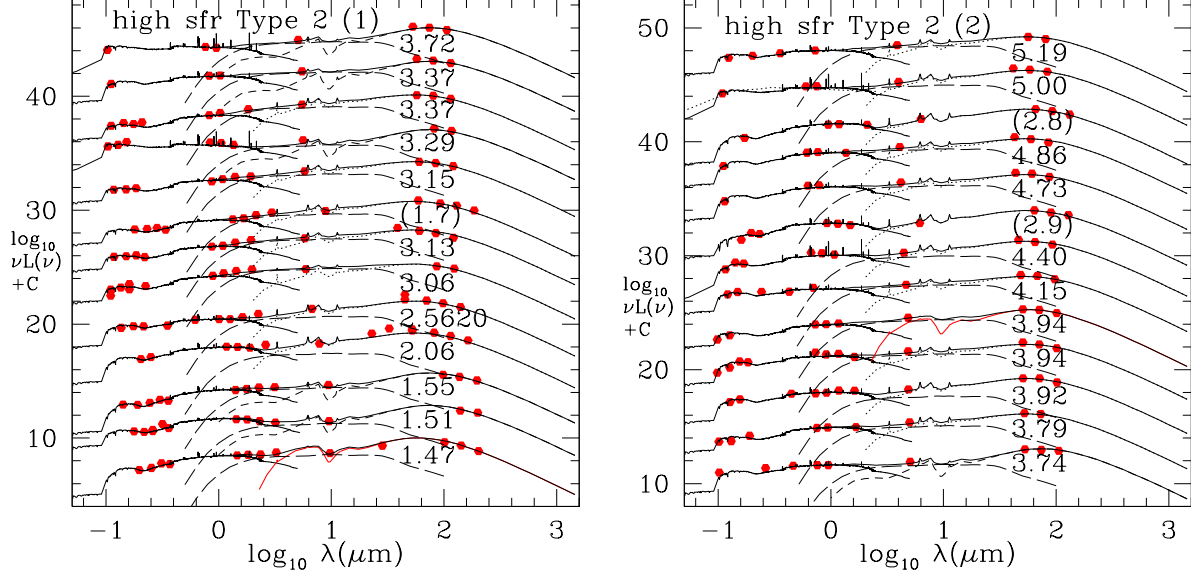


Figure 5. SEDs of Lockman-SPIRE 500 μm sources with extremes starburst luminosities labelled with the redshift, midir requiring AGN dust torus template. Lower redshift aliases (z_{comb}) are shown with redshift bracketed, above SED for the higher redshift alias. Dotted loci: M82 starburst, dashed loci: Arp 220 starburst, long-dashed loci: AGN dust torus, red loci: young starburst template.

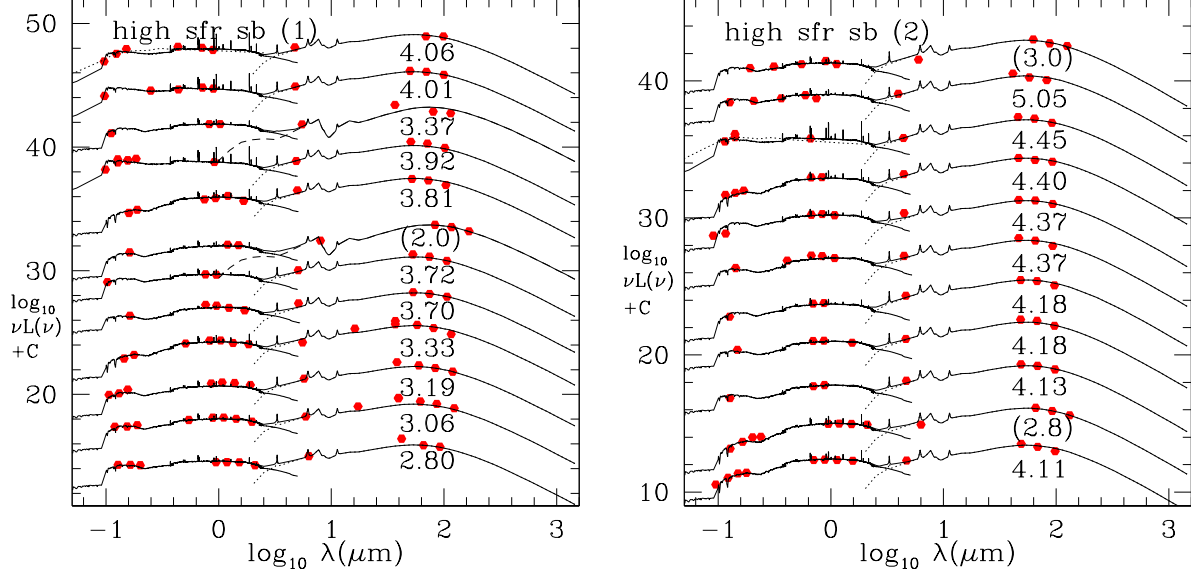


Figure 6. SEDs of Lockman-SPIRE 500 μm sources with extremes starburst luminosities labelled with the redshift, farir-submm fitted with M82 or A220 starburst templates. Lower redshift aliases (z_{comb}) are shown with redshift bracketed, above SED for the higher redshift alias. Dotted loci: M82 starburst, dashed loci: Arp 220 starburst, long-dashed loci: AGN dust torus, red loci: young starburst template.

growth. However at recent epochs star-formation is mainly fed by accretion from the cosmic web, by minor mergers and interactions, and by spiral density waves, so is taking place further from the galactic nucleus. This uncouples the direct connection between star-formation and black-hole growth. The gas feeding the black hole is fed to the galactic nucleus more gradually and may include gas fed by mass-loss from stars. It is still surprising that it is so much easier to feed a black hole at the present epoch than it is to form stars.

Shallower evolution for AGN compared to that for starbursts was found for source-count models in which different types of object were allowed different rates of evolution (Rowan-Robinson 2009).

It is possible that the high proportion of AGN amongst these extreme starbursts is pointing to the influence of AGN-jet-induced star formation in these extreme objects (Klamer et al 2004, Clements et al 2009). The time-scales for these starbursts and the time-scale for black hole growth are re-

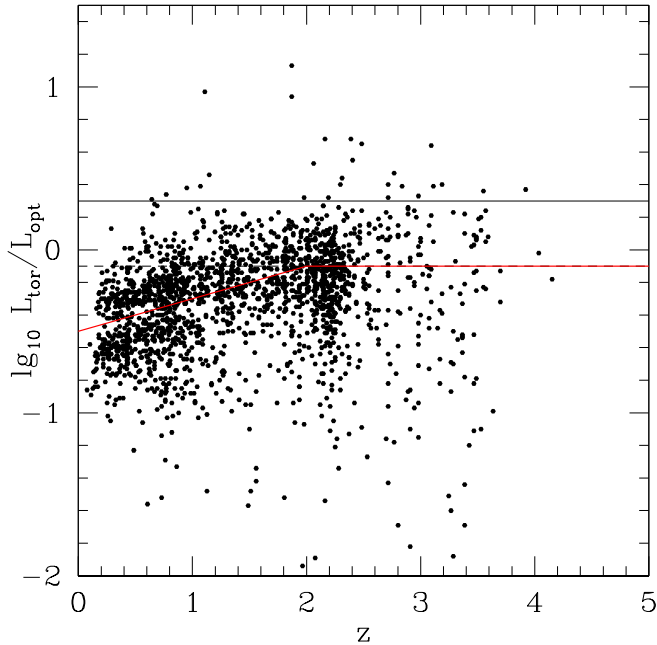


Figure 7. $\log_{10} L_{\text{tor}}/L_{\text{opt}}$ versus z for QSOs in SWIRE Photometric Redshift Catalogue. Solid black line corresponds to $L_{\text{tor}} = L_{\text{bh}}$, for assumed optical bolometric correction of 2.0. Red line shows assumed dependence of dust torus covering factor on redshift.

markedly well matched at a few $\times 10^7$ yrs (cf Rigopoulou et al 2009). However the greatly enhanced gas supply to the nucleus associated with violent mergers may be a sufficient explanation.

The SWIRE-Lockman area includes the CLASX X-ray survey and Rowan-Robinson et al (2009) gave a detailed discussion of the associations of CLASX and SWIRE sources. Only 2 of the 400 CLASX-SWIRE sources are detected by *Herschel*-SPIRE. While AGN are present in the *Herschel* submillimetre galaxy population, they make a negligible contribution to the submillimetre flux.

6 CONCLUSIONS

After careful exclusion of lensed galaxies and blazars, we have identified samples of extreme starbursts, with star-formation rates in the range $5000\text{--}30,000 M_{\odot}/\text{yr}$, from the IRAS-FSS $60 \mu\text{m}$ galaxy catalogue (RIFSCz) and from the *Herschel*-SWIRE (HerMES) $500 \mu\text{m}$ survey. There do not seem to be any genuine cases with $\text{SFR} > 30,000 M_{\odot}/\text{yr}$ and this may be essentially an Eddington-type limit. The SEDs of 58 HerMES extreme starbursts have been modelled in detail. The photometric redshifts are, in almost all cases, supported by redshift estimates from the $250\text{--}500 \mu\text{m}$ colours. Using dust mass as a proxy for gas mass, extreme starbursts are found to be very gas rich systems, which will double their stellar mass in $0.3\text{--}3 \times 10^8$ yrs.

About half of the *Herschel* extreme starburst systems also contain an AGN, but in no case do these dominate the bolometric output. With assumptions about the Eddington ratio and accretion efficiency, we find a universal rela-

tion between black-hole mass and total stellar mass, with $M_{\text{bh}} \sim 0.001 M_{*}$. This is driven by the episode of extreme star-formation and black hole growth at $z=2\text{--}5$. But while the star formation rate has fallen by a factor of 1000 between redshift 5 and the present epoch, the black hole accretion rate has fallen by a factor of only 30, suggesting a decoupling between star formation and the feeding of the nuclear black hole.

7 ACKNOWLEDGEMENTS

Herschel is an ESA space observatory with science instruments provided by European-led Principal Investigator consortia and with important participation from NASA. SPIRE has been developed by a consortium of institutes led by Cardiff University (UK) and including Univ. Lethbridge (Canada); NAOC (China); CEA, LAM (France); IFSI, Univ. Padua (Italy); IAC (Spain); Stockholm Observatory (Sweden); Imperial College London, RAL, UCL-MSSL, UKATC, Univ. Sussex (UK); and Caltech, JPL, NHSC, Univ. Colorado (USA). This development has been supported by national funding agencies: CSA (Canada); NAOC (China); CEA, CNES, CNRS (France); ASI (Italy); MCINN (Spain); SNSB (Sweden); STFC, UKSA (UK); and NASA (USA).

REFERENCES

- Aguirre P., Baker A.J., Menanteau F., Lutz D., Tacconi L., 2013, *ApJ* 768, 164
- Asboth V. et al, 2016, *MNRAS* 462, 1989
- Barnett R. et al, 2015, *AA* 575, A31
- Blain A.W., Smail I., Ivison R.J., Kneib J.-P., Frayer D.T., 2002, *Phys.Reports* 369, 111
- Chakrabarti S. et al, 2008, *ApJ* 688, 972
- Chen C. et al, 2015, *ApJ* 799, 194
- Chen B., Xinyu D., Kochanek C.S., Chartas G., 2013, *astro-ph:1306.0008*
- Clements D.L. et al, 2009, *ApJ* 698, L188
- Clements D.L. et al, 2010, *AA* 518, L8
- Daddi E. et al, 2010, *ApJ* 713, 686
- Dowell C.D. et al, 2014, *ApJ* 780, 75
- Elmegreen B.G., 1983, *MNRAS* 203, 1011
- Efstathiou A., Rowan-Robinson M., Siebenmorgen R., 2000, *MNRAS* 313, 734
- Efstathiou A., Rowan-Robinson M., 2003, *MNRAS* 343, 322
- Farrah D., Verma A., Oliver S., Rowan-Robinson M., McMahon R., 2002, *MNRAS* 329, 605
- Franceschini A. et al, 1991, *AA Supp* 89, 285
- Griffin M.J. et al, 2010, *AA* 518, L3
- Gruppioni C. et al, 2013, *MNRAS* 432, 23
- Gruppioni C. et al, 2015, *MNRAS* 451, 3419
- Hayward C. et al, 2011, *ApJ* 743, 159
- Henriques B.M.B., White S.D.M., Thomas P.A., Angule P., Guo Q., Lemson G., Springel V., Overzier R., 2015, *MNRAS* 451, 2663
- Hopkins P. et al, 2010, *MNRAS* 402, 1693
- Houck J.R. et al, 1985, *ApJ* 290, L5
- Ivison R.J. et al, 2012, *MNRAS* 425, 1320

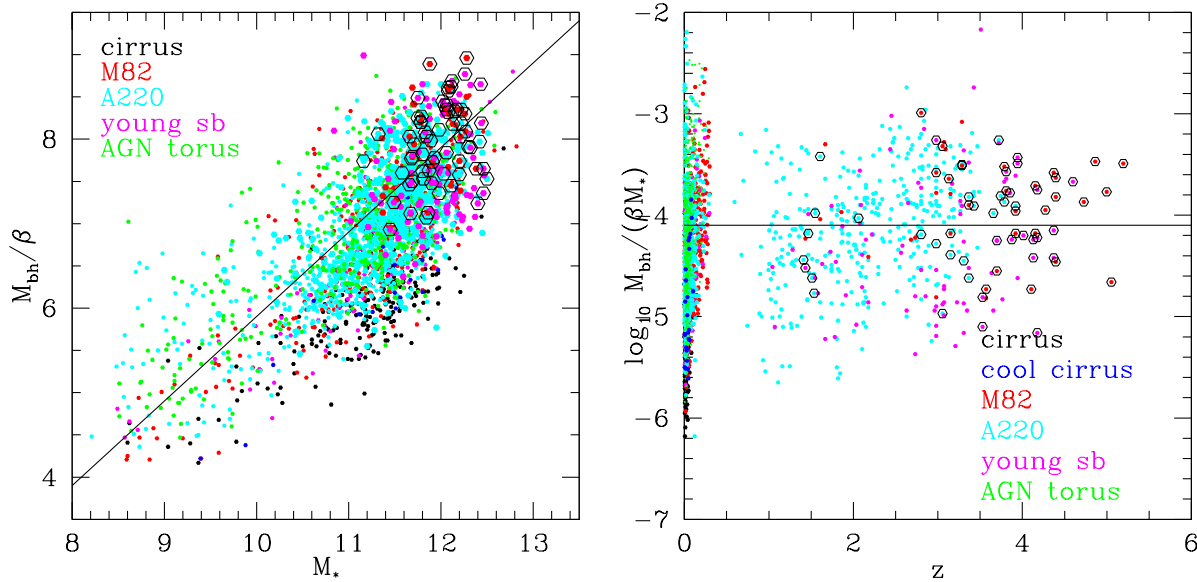


Figure 8. L: Black-hole mass, M_{bh}/β^{-1} , versus total stellar mass, M_* , for HerMES-SWIRE sources and for RIFSCz sources with $z < 0.3$ (smaller points), with AGN dust tori. QSOs are excluded by the requirement that there be a stellar mass estimate, so these are all Type 2 AGN. Circled points are *Herschel* extreme starbursts. R: $M_{bh}/(\beta M_*)$ versus z for HerMES-SWIRE sources and for RIFSCz sources with $z < 0.3$, with AGN dust tori.

Kelly B.C., Vestergaard M., Fan X., Hopkins P., Hernquist L., Siemiginowska A., 2010, *ApJ* 719, 1315
 Kormendy J., Ho L.C., 2013, *ARAA* 51, 511
 Lacey C.G. et al, 2016, *MNRAS* 462, 3854
 Laigle C. et al, 2016, *ApJS* 224, 24
 Lapi A., Mancuso C., Celotti A., Danese L., 2017, *ApJ* 835, 37
 Magdis G.E. et al, 2011, *ApJ* 740, L14
 Madau P. and Dickinson M., 2014, *ARAA* 52, 415
 Magorrian J. et al, 1998, *AJ* 115, 2285
 Murray N., Quataert E., Thompson T.A., 2005, *ApJ* 618, 569
 Oliver S.J. et al, 2010, *AA* 518, L21
 Oliver S.J. et al, 2012, *MNRAS* 424, 1614
 Partridge R.B., Peebles P.J.E., 1967, *ApJ* 147, 868
 Afonso-Luis A., 2013, *MNRAS* 428, 291
 Pearson W.J., Wang L., van der Tak F.F.S., Hurley P.D., Burgarella D., Oliver S.J., 2017, *AA* (in press)
 Pitchford L.K. et al, 2016, *MNRAS* 462, 4067
 Rigopoulou D. et al, 2009, *MN* 400, 1199
 Rodighiero G. et al, 2011, *ApJ* 739, 40L
 Rodighiero G. et al, 2014, *MNRAS* 443, 19
 Rowan-Robinson M. et al, 2008, *MNRAS* 386, 697
 Rowan-Robinson M. et al, 2010, *MNRAS* 409, 2
 Rowan-Robinson M. et al, 2013, *MNRAS* 428, 1958
 Rowan-Robinson M. et al, 2014, *MNRAS* 445, 3848
 Rowan-Robinson M. et al, 2016, *MNRAS* 461, 1100
 Rowan-Robinson M., Clements D.L., 2015, *MNRAS* 453, 2050
 Rowan-Robinson M., Valtchanov I., Nandra K., 2009, *MN* 397, 1326
 Rowan-Robinson M., Wang L., 2010, *MNRAS* 406, 720
 Rowan-Robinson M., Wang L., 2015, *Publications of the Korean Astr. Soc.* (in press), astro-ph 1505.03797
 Salpeter E.E., 1964, *ApJ* 140, 796

Scoville N. et al, 2001, *AJ* 122, 3017
 Schulz B. et al, 2017, *SPIRE Point Source Catalog Explanatory Supplement* (IPAC, Caltech)
 Scoville N. et al, 2007, *ApJS* 172, 1
 Scoville N. et al, 2016, *ApJ* 820, 83
 Soifer B.T. et al, 1984, *ApJ* 283, L1
 Steinhardt C.L., Elvis M., 2009, *MNRAS* 402, 2637
 Tacconi L. et al, 2010, *Nature* 463, 781
 Tacconi L. et al, 2013, *ApJ* 768, 74
 Wang L., Rowan-Robinson M., 2010, *MNRAS* 401, 35
 Wang L. et al, 2014a, *MNRAS* 444, 2870
 Wang L., Rowan-Robinson M., Norberg P., Heinis S., Han J., 2014b, *MNRAS* 442, 2739
 Weedman D.W., Houck J.R., 2008, *ApJ* 686, 127
 Wiklind T. et al, 2014, *ApJ* 785, 111

8 APPENDIX

Figure 10 shows the star-formation rate functions for $z = 0.75-3.25$ derived using the new $24 \mu\text{m}$ normalisation (section 3 above). The tendency of the bright end of the function to be overestimated relative to the model fits (see Fig 9 of Rowan-Robinson et al 2016) has disappeared. The new parametric fits give star-formation rate densities that differ from the values of Rowan-Robinson et al (2016) by $< 1\sigma$.

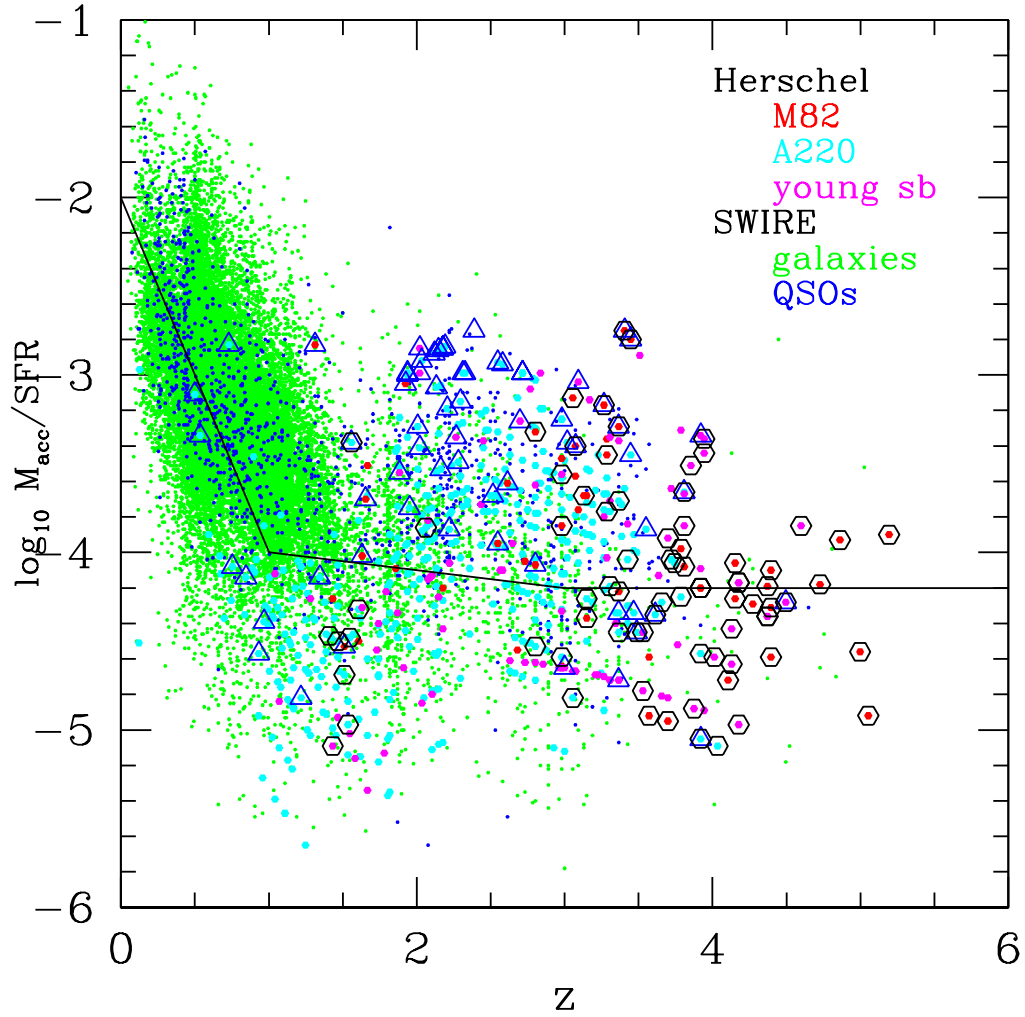


Figure 9. $\log_{10} M_{\text{acc}}/SFR$ versus z for SWIRE and HerMES sources. Circled points are extreme starburst and blue open triangles denote QSOs.

Table 4. Star-formation rate density

$z =$	0.75	1.25	1.75	2.25	2.75	3.25
old sfrd	-1.28	-0.95	-1.06	-1.05	-0.82	-0.99
	± 0.21	± 0.11	± 0.13	$+0.27, -0.09$	$+0.18, -0.36$	$+0.29, -0.46$
new sfrd	-1.29	-1.05	-1.12	-0.97	-0.99	-0.92

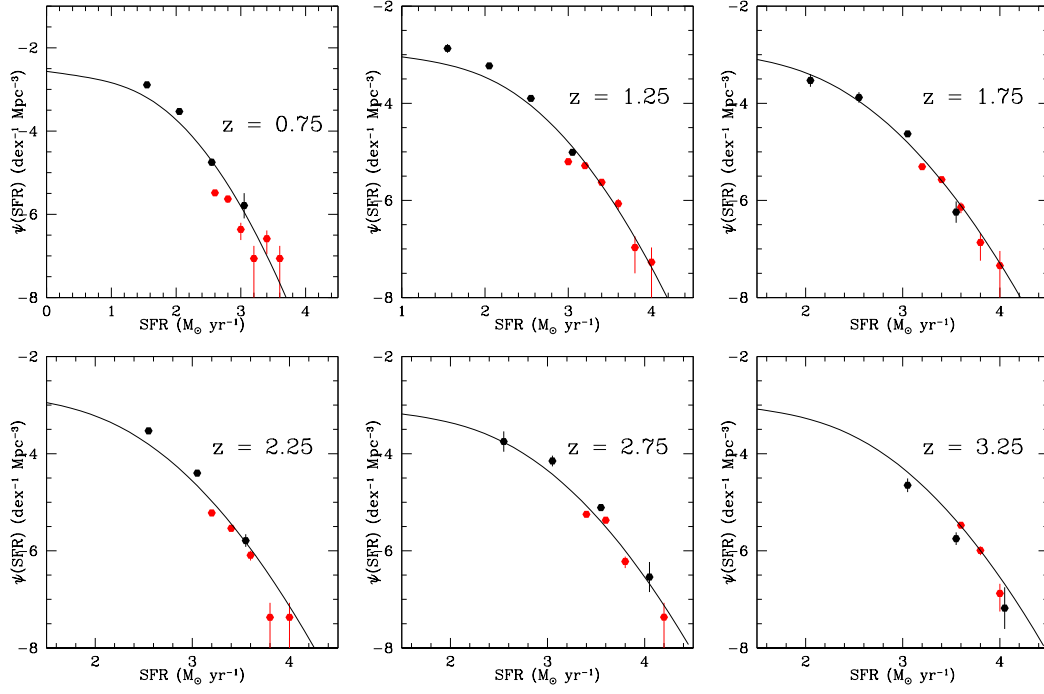


Figure 10. Revised star-formation rate functions for $z = 0.25$ - 3.25 , with $24 \mu\text{m}$ normalisation.

Table 5. Extreme starbursts: QSOs and Type 2 AGN

RA	dec	i	S24 (μ Jy)	S250 (mJy)	S350 (mJy)	S500 (mJy)	z_{phot}	type	χ^2	n_b	z_{sbm}	z_{cmb}	SFR
QSO	Fig 4L												
9.62462	-43.74844	R=17.45	11957	106.7	83.0	54.5	1.5670	QSO	2.9	9	2.40	2.39	4.02
164.96553	58.30081	19.44	5479.0	43.8	48.7	34.2	2.3350	QSO	13.6	11	2.33	3.47	3.94
36.84426	-5.31016	19.35	1963.8	52.7	45.4	36.7	3.07	QSO	42.1	14	3.01	3.07	3.80
164.64154	58.09799	20.95	1386.3	44.9	45.4	28.0	3.37	QSO	2.1	11	2.01	3.07	3.72
162.77605	58.52327	22.32	184.6	54.5	53.0	41.1	3.47	QSO	3.2	8	3.19	3.37	3.70
161.85410	57.91928	21.11	245.8	76.1	80.3	65.3	3.49	QSO	1.3	10	3.42	3.47	3.87
162.20728	58.28162	21.59	205.5	56.6	57.7	40.3	3.61	QSO	8.5	19	3.14	3.37	3.85
161.36092	58.03157	20.67	428.6	-	37.5	41.2	3.81	QSO	5.2	11	5.05	3.90	3.84
162.52769	57.28142	21.62	145.4	106.3	100.1	61.7	3.92	QSO	8.4	8	1.93	1.95	4.07
							1.95	QSO					3.47
162.68120	57.55606	g=24.35	194.9	25.5	37.0	38.3	4.50	QSO	1.3	3	4.79	4.50	3.80
Type 2 AGN	Fig 5L												
33.71100	-4.17344	22.53	1016.3	96.2	69.0	32.5	1.47	Scd	9.3	6	1.92	1.57	3.82
8.04056	-43.71930	R=23.01	612.3	73.8	71.4	51.2	1.51	Sab	26.4	7	2.96	2.09	3.75
35.11776	-5.50099	23.55	864.4	72.2	65.1	45.2	1.55	Scd	9.0	7	2.74	2.02	3.78
162.91730	58.80596	22.03	1964.8	183.8	133.1	78.7	2.06	Sab	45.6	6	2.11	2.09	3.75
2 161.75087	59.01883	23.66	1329.6	75.0	61.0	40.6	2.5620	Scd	1.7	7	2.53	2.89	3.75
9.17274	-43.34398	R=23.65	2800.6	71.5	65.3	38.7	3.06	Sab	15.7	6	1.84	2.47	3.79
35.49809	-5.92264	23.57	1341.4	62.8	55.9	30.7	3.13	Sab	1.9	6	2.49	1.69	3.78
							1.7	Sab					3.29
35.95578	-5.08144	23.85	1002.1	71.2	77.6	59.5	3.15	Sab	7.3	5	3.32	3.27	3.80
10.23271	-44.07592	R=21.50	487.0	75.3	68.1	45.7	3.29	sb	13.3	5	2.67	3.07	3.72
36.15258	-5.10250	24.92	627.2	43.5	53.7	41.5	3.37	Sab	2.0	5	3.60	3.47	3.71
162.38754	57.70547	g=24.13	519.3	65.7	65.0	56.3	3.37	Scd	1.6	3	3.47	3.37	3.74
159.78395	58.55888	g=24.41	231.6	35.3	39.9	36.7	3.72	Sdm	0.0	3	3.91	3.68	3.80
	Fig 5R												
163.98088	57.81277	g=24.66	213.9	27.8	34.6	41.0	3.74	Scd	4.4	5	5.03	3.68	3.79
36.96840	-5.02193	24.92	610.3	40.4	47.8	39.3	3.79	Sab	7.5	6	3.66	3.79	3.95
160.85139	58.02007	23.22	443.7	43.1	61.2	37.4	3.92	Sbc	2.6	5	2.24	3.37	3.93
35.11967	-5.73062	22.40	945.3	58.8	58.9	38.8	3.94	Sbc	14.8	6	2.90	1.69	3.83
35.92307	-4.73225	25.55	849.5	48.5	59.5	45.3	3.94	Sab	2.9	5	3.56	3.57	3.83
164.28366	58.43524	22.30	596.0	43.5	51.0	37.4	4.15	Scd	60.0	5	2.46	3.79	4.11
161.63013	59.17688	23.94	391.4	-	29.6	27.0	5.19	Scd	4.8	4	3.05	4.75	4.22
8.70199	-44.48560	R=25.38	423.0	31.2	36.1	27.1	4.73	Scd	0.01	3	3.45	3.47	4.23
9.30474	-43.03506	R=25.19	504.5	39.6	36.3	26.3	4.86	Scd	0.09	3	2.87	2.80	4.24
							2.8	Scd					3.84
9.19681	-44.42382	R=24.35	249.1	39.2	43.2	41.0	5.00	sb (QSO?)	0.04	3	3.89	4.13	4.20
34.53469	-5.00769	23.47	342.8	47.3	42.4	35.8	4.40	sb	4.0	5	3.18	3.17	4.04
							2.9						

Table 6. Extreme starbursts: young starbursts, M82 and A220 type starbursts

RA	dec	i	S24	S250	S350	S500	z_{phot}	type	χ^2	n_{bands}	z_{subm}	z_{comb}	sfr
young sbs	Fig 4R												
159.03456	58.44533	21.37	1127.8	131.6	84.2	42.2	1.44	Scd	4.8	4	1.16	1.19	3.79
162.26817	58.46461	22.33	504.1	85.4	78.7	62.8	3.15	Sbc	5.0	6	3.16	3.17	3.87
160.33716	59.40493	22.36	1225.7	-	36.8	39.0	3.29	Scd	6.7	6	4.93	3.27	3.72
160.50839	58.67179	23.49	904.6	95.7	79.5	60.5	3.81	Sab	4.1	6	2.86	3.07	4.00
36.59817	-4.56164	25.11	389.5	59.3	67.2	54.7	3.88	Sab	2.1	5	3.53	3.68	3.83
36.10986	-4.45889	24.59	828.6	88.4	89.5	67.0	3.92	Sab	2.0	5	3.14	3.27	4.20
161.98271	58.07477	22.10	264.4	44.2	45.3	33.6	4.13	sb	25.4	6	3.15	3.68	3.76
M82, A220	Fig 6L												
162.33324	58.10657	22.61	516.4	56.9	52.9	59.6	2.80	Scd	6.1	8	4.09	2.89	3.73
160.91940	57.91475	22.32	682.3	116.5	102.0	65.4	3.06	Sab	20.5	6	2.56	2.80	4.05
8.81979	-42.69724	R=22.90	706.2	87.4	74.6	53.9	3.19	Scd	6.1	5	2.72	2.98	3.72
161.21138	58.11261	23.29	560.2	148.6	116.4	54.2	3.33	Sbc	26.8	5	2.02	1.75	3.70
160.16505	57.27072	23.12	625.2	52.7	52.4	44.8	3.70	Sab	31.2	4	3.45	3.68	3.81
159.67438	58.55686	g=24.34	299.1	58.1	53.7	35.4	3.72	Scd	0.0	3	2.68	2.02	3.78
							2.0	Scd					3.35
35.33492	-5.74307	24.94	799.9	69.9	74.9	45.5	3.81	Sbc	2.7	4	2.06	2.09	4.10
164.55716	58.65286	21.85	176.9	67.4	66.7	43.6	3.92	sb	2.3	6	2.96	3.57	4.04
159.95905	57.18814	g=24.01	232.5	-	36.5	37.9	3.37	Scd	0.1	3	4.88	3.37	3.73
162.84616	58.00514	g=24.41	179.3	34.4	40.1	32.4	4.01	sb	13.0	5	3.56	4.01	3.71
162.46065	58.11701	21.96	252.5	-	28.4	41.4	4.06	sb (QSO?)	7.9	6	4.81	4.13	3.88
	Fig 6R												
35.73369	-5.62305	23.42	422.0	73.1	60.9	42.1	4.11	Sbc	4.1	6	2.61	2.80	4.07
							2.8	Sbc					3.77
7.98209	-43.29812	R=24.87	275.8	45.6	49.7	38.8	4.13	Sab	0.02	3	3.37	3.37	3.81
164.52054	58.30782	23.40	306.9	81.9	92.1	58.2	4.18	Sab	0.03	3	2.16	3.07	3.91
9.28433	-44.23750	R=25.06	437.0	62.5	72.5	51.5	4.18	Scd	0.03	3	2.40	2.39	3.95
161.89894	58.16401	23.60	315.0	66.4	59.7	35.3	4.37	Sab	22.7	4	1.82	2.89	3.96
35.73605	-4.88950	g=25.02	421.5	40.6	51.9	40.5	4.37	Scd	11.4	6	3.69	2.55	4.09
36.65871	-4.14628	24.91	288.8	46.1	45.7	48.1	4.40	Sbc	2.1	6	3.92	4.01	4.03
162.42290	57.18750	22.25	121.0	43.5	46.1	32.6	4.45	sb (QSO?)	5.6	4	3.22	4.37	3.74
161.58835	59.65826	23.71	156.0	48.1	35.1	31.8	5.05	Scd	4.7	5	3.03	2.98	4.07
							3.0						
z_{comb}	preferred,	SED not shown											
159.24428	57.85775	22.68	281.7	85.7	64.4	27.3	3.06	Scd	3.1	5	1.80	1.51	3.72
162.55945	57.19608	22.12	315.3	74.6	56.8	26.9	3.70	sb	3.6	5	2.01	1.19	3.77
162.52769	57.28142	21.62	145.4	106.3	100.1	61.7	3.92	QSO	8.4	8	1.93	195	4.07
164.02647	52.07153	22.28	252.3	43.2	35.2	26.0	4.18	sb	2.5	4	2.74	1.82	3.71
9.08571	-45.59628	R=24.89	271.8	95.7	76.3	41.3	4.25	Scd	0.85	3	2.33	2.09	4.00
9.11142	-42.84052	R=24.44	354.5	37.6	45.0	30.1	4.60	Scd	0.03	3	2.36	2.31	3.95
34.26031	-4.95556	24.95	451.0	55.2	61.6	35.6	4.15	Sbc	3.9	4	2.03	21.6	4.05
36.25277	-5.59534	23.94	511.7	57.9	42.0	33.6	4.27	Scd	1.2	5	2.65	1.95	4.17